High accuracy proton relative stopping power measurement

van Abbema, J. K.; van Goethem, M. -J.; Mulder, J.; Biegun, A. K.; Greuter, M. J. W.; van der Schaaf, A.; Brandenburg, S.; van der Graaf, E. R.

Published in:
Nuclear Instruments & Methods in Physics Research Section B-Beam Interactions with Materials and Atoms

DOI:
10.1016/j.nimb.2018.09.015

Publication date:
2018

Nuclear Inst. and Methods in Physics Research B 436 (2018) 99–106

Contents lists available at ScienceDirect

Nuclear Inst. and Methods in Physics Research B

journal homepage: www.elsevier.com/locate/nimb

High accuracy proton relative stopping power measurement

J.K. van Abbema[a], M.-J. van Goethem[a,b], J. Mulder[a,b], A.K. Biegun[a], M.J.W. Greuter[c], A. van der Schaaf[b], S. Brandenburg[a], E.R. van der Graaf[a,*]

[a] University of Groningen, KVI – Center for Advanced Radiation Technology, Zernikelaan 25, 9747 AA Groningen, The Netherlands
[b] University of Groningen, University Medical Center Groningen, Department of Radiation Oncology, PO Box 30.001, Groningen, The Netherlands
[c] University of Groningen, University Medical Center Groningen, Department of Radiology, PO Box 30.001, Groningen, The Netherlands

ARTICLE INFO

Keywords:
Proton therapy
Relative stopping powers
High accuracy proton range measurement

ABSTRACT

Proton therapy is a fast growing treatment modality for cancer and is in selected cases preferred over conventional radiotherapy with photons because of the highly conformal dose distribution that can be achieved with protons due to their steep dose gradients. However, these steep gradients also make proton therapy sensitive to range uncertainties. Proton ranges are calculated from proton stopping powers relative to that in water (Relative Stopping Power, RSP). The RSPs needed for a treatment plan can be estimated from CT (Computed Tomography) data of a patient. High accuracy reference values of RSPs are required to assess the accuracy of these CT based estimates. In this paper we present a water phantom that enables accurate measurement of depth dose profiles in water. Experimental RSPs with a relative standard uncertainty smaller than 0.4% (1σ) for samples with a water equivalent thickness of about 2 cm can be derived from the measured depth dose distributions. Most CT based RSP estimates use an approximate RSP model based on the Bethe-Bloch formula without the shell, density, Barkas and Bloch correction. In the Geant4 Monte Carlo code these corrections are included and RSP calculations with this code are expected to be more accurate. In this work, a set of 32 well defined (composition and density), mostly clinically relevant materials is used to assess the correspondence between RSPs that were measured, that were estimated from the approximate RSP model and that were calculated from Monte Carlo simulations. With the measured RSPs we provide a ground-truth bench mark to test the validity of RSPs derived from CT imaging and Monte Carlo simulations.

1. Introduction

The potential advantage of protons over conventional radiation modalities (photons, electrons) for radiotherapy of cancer was first mentioned by Wilson in 1946 [1]. Protons have a finite range and local high dose region which facilitate a higher conformity to the tumor and less dose to the surrounding healthy tissues as compared to conventional irradiation with photons. Accurate positioning of the local high dose region is critical for exploiting the benefit of protons over photons. In proton therapy, each tissue is characterized by a proton stopping power relative to water (relative stopping power, RSP) that is derived from X-ray computed tomography (CT) data of the patient. Uncertainties in these RSPs introduce range uncertainties which have to be taken into account in treatment planning by using safety margins. These safety margins reduce the possibility to fully exploit the advantage of proton irradiations by limiting beam angles and increasing dose to healthy and sometimes critical tissues surrounding the tumor. Different methods have been proposed to derive RSPs from CT data of the patient. Single energy CT (SECT) methods typically correlate measured CT numbers to RSPs based on calculated CT numbers and RSPs for tissue substitutes or average tissue compositions [2,3]. Dual energy CT (DECT) provides measured CT numbers for two different spectral photon distributions and allows determination of the relative electron density and an effective atomic number [4–10]. RSPs can be calculated from the measured relative electron density and a relation between this effective atomic number and the mean excitation energy in the Bethe-Bloch formalism for calculation of stopping powers [10,11]. To assess the validity of the different CT-based methods for calculation of RSPs an accurate method for measurement of RSPs is needed.

In this paper we introduce an accurate method to derive RSPs from measured depth dose distributions using a water phantom in a proton beamline. Measured RSP's are presented for a set of 32 well defined (composition and density), mostly clinically relevant materials. These measured RSPs are used as ground-truth values to assess the accuracy of the Bethe-Bloch formula without the higher order corrections and of Geant4 Monte Carlo simulations to predict RSPs.

* Corresponding author.
E-mail address: vandergraaf@kvi.nl (E.R. van der Graaf).

https://doi.org/10.1016/j.nimb.2018.09.015
Received 19 July 2018; Received in revised form 6 September 2018; Accepted 6 September 2018
Available online 13 September 2018
0168-583X/

2. Materials and methods

2.1. Accuracy of stopping power calculations based on the Bethe-Bloch equation

The total proton stopping power is due to energy transfer of the proton to the electrons (electronic stopping) and to the nuclei (nuclear stopping) of the target material. Electronic stopping causes ionization and excitation of target atoms and energy loss of the proton. Nuclear stopping changes the direction of the proton and the intensity of the incoming proton beam but contributes less than 0.1% to the total stopping power above 0.4 MeV [12] and is thus not relevant for range calculations. The Bethe-Bloch formula that describes the electronic stopping power of protons can be expressed as [13,14]

$$S = -\frac{dE}{dx} = \left(\frac{4\pi r_e^2 m_e c^2}{\beta^2}\right)\left(N_A \rho \frac{Z}{A}\right) L(\beta) \tag{1}$$

with r_e the classical electron radius and $m_e c^2$ the electron rest energy with c the speed of light in vacuum. The first factor in the energy loss is proportional to $1/\beta^2$ with $\beta = v/c$ and v the proton velocity. The second factor is the electron density of the target material ρ_e, which equals $N_A \rho Z/A$ with mass density ρ, Avogadro's number N_A, atomic number Z and atomic weight A. The last factor is the stopping number $L(\beta)$, which is the sum of the primary stopping number L_0, the Barkas correction L_1, the Bloch correction L_2 and higher order corrections which are negligible compared to L_1 and L_2.

$$L(\beta) = L_0(\beta) + L_1(\beta) + L_2(\beta) + \cdots \tag{2}$$

The primary stopping number L_0 can be expressed as

$$L_0(\beta) = f(\beta) - \ln\langle I\rangle - \frac{C}{Z} - \frac{\delta}{2} \tag{3}$$

where $f(\beta)$ is defined as

$$f(\beta) = \ln\left(\frac{2m_e c^2 \beta^2}{1-\beta^2}\right) - \beta^2 \tag{4}$$

The mean excitation energy term $\ln\langle I\rangle$ takes into account the electronic structure of the target material. The mean excitation energy $\langle I\rangle$ is defined as the effective value (averaged over all possible electron states (ionization, vibration and excitation)) of the minimum energy transfer in a collision. The shell correction term C/Z addresses the fact that when the proton velocity decreases from relativistic energies the proton velocity is no longer much larger than the bound electron velocity as required for the Bethe-Bloch theory to be valid. The density effect term $\delta/2$ corrects for polarization effects in the target material, reducing the stopping power by a decrease of the assumed free-space electromagnetic field of the proton by the dielectric constant of the target material [14]. We have estimated from information in the literature the relative importance of the different correction terms with respect to the term $f(\beta) - \ln\langle I\rangle$.

Shell corrections (C/Z) become especially important for the inner shell electrons of the heavier elements. They have been calculated using hydrogenic wave functions [15] or the local density approximation [13]. Both methods seem to give consistent results. Low Z elements have the smallest correction. For elements most relevant for proton therapy ($Z < 20$) the absolute value of the correction term is around 0.15 between 1 and 10 MeV and decreases to < 0.1 between 10 and 40 MeV and < 0.05 between 40 and 250 MeV. This corresponds to a relative decrease of the stopping power of 3–4% for energies between 1 and 10 MeV and approximately 1–1.5% between 10 and 40 MeV and < 1% for energies between 40 and 250 MeV.

The density effect ($\delta/2$) only becomes relevant if the kinetic energy of the proton exceeds its rest energy and is therefore of limited importance for clinically used proton energies (up to 250 MeV). The absolute contribution of the density effect is estimated (from Fig. 11 in [13]) to be smaller than 0.01 for all elements and energies below 200 MeV. Because $f(\beta) - \ln\langle I\rangle$ is larger than 5 for Z between 1 and 20 and energies larger than 10 MeV this implies a correction < 0.2% to the stopping power.

The Barkas correction (L_1) corrects for the higher density of target electrons in the vicinity of the positively charged proton. For low energy protons this effect becomes important because the target electrons have time to move towards the stopping protons. Ashley et al. [16] derived an empirical formula for low energy projectiles to approximate this effect. This formula was used by Bichsel [12] who reports a Barkas correction of 0.36% for 10 MeV protons on aluminium. Using the empirical approach of Ziegler (Eq. 35 in [13]) we estimate that the Barkas correction is smaller than 0.9% for energies above 10 MeV for Z between 1 and 20.

The Bloch correction (L_2) originates from close collisions of protons with target electrons and mostly depends on the proton energy and little on the target material. From Eq. (5) from Bichsel [12] we conclude that the Bloch correction is smaller than 0.2% for energies between 5 and 10 MeV and < 0.1% above 10 MeV.

Bragg and Kleeman [17] proposed an additivity rule for mass stopping powers S/ρ of elements to determine the mass stopping power of a mixture or compound. Following this Bragg additivity rule the mean excitation energy $\ln\langle I\rangle$ of a compound can be approximated by

$$\ln\langle I\rangle = \frac{\sum_k \omega_k \frac{Z_k}{A_k} \ln\langle I_k\rangle}{\sum_k \omega_k \frac{Z_k}{A_k}} \tag{5}$$

with the mass fraction ω_k and mean excitation energy $\langle I_k\rangle$ of element k in the compound. The validity domain and the accuracy of the Bragg additivity rule have not been well established. The Bragg additivity rule does not account for different states of aggregation and chemical binding between atoms in a molecule. The effect of the state of aggregation is for water (vapor, liquid or ice) the largest for proton energies of 50–100 keV [18]. From core and bond corrections applied in the software package SRIM [14] to account for chemical binding we conclude that the corrections may amount to 6–7% in the stopping region (up to 1 MeV) and are applied as a constant (energy independent) scaling factor. For energies above 3–4 MeV no corrections are applied in SRIM. The uncertainty in the $\langle I\rangle$ values of the elements is difficult to estimate but experiments suggest that tabulated elemental$\langle I\rangle$ values [19,20] are too low for the elements [21], leading to underestimation of $\langle I\rangle$ values for compounds when calculated with the Bragg additivity rule [22].

The range of a 10 MeV proton in water in the continuous slowing down approximation (CSDA) is 1.23 mm and this decreases rapidly for lower energies: for 5 MeV protons it has already decreased to 0.36 mm [23]. Consequently, for energies below 10 MeV, correction terms which contribute less than 10% (equivalent to 0.1 mm water) are not relevant for the total range prediction with the Bethe-Bloch formula. The overall contribution of the correction terms is dominated by the shell correction which amounts −1.5 to −1% for energies between 10 and 40 MeV and −1 to 0% between 40 and 250 MeV. The Barkas correction contributes < 1% above 10 MeV. These corrections partly cancel out due to their respectively negative and positive sign. As the higher energies contribute most to the range (40 MeV protons have a CSDA range of only 1.49 cm [23]), the total effect on the range of all correction terms is estimated to be less than 1–1.5% for protons with clinically relevant energies.

Consequently, the electronic stopping power of a material can be approximated within this estimated accuracy of 1–1.5% by

$$S = -\frac{dE}{dx} = \frac{4\pi r_e^2 m_e c^2}{\beta^2} \rho_e \left(f(\beta) - \ln\langle I\rangle\right) \tag{6}$$

provided the value used for $\langle I\rangle$ is correct.

The electronic stopping power relative to water (relative stopping power, RSP) can then be approximated by

Table 1
Compositions (weight percentages) and mass densities ρ(at 23.8 °C) of the 32 sample materials. Materials No. 1–6 and 24–32 are solids and 7–23 are liquids.

No.	Material	Ch. formula	Z	1	6	7	8	9	12	13	14	17	19	20	25	ρ
			A	1.008	12.011	14.007	15.999	18.998	24.305	26.982	28.086	35.453	39.098	40.078	54.938	[g cm^{-3}]
1	LN-450 Lung			8.47	59.56	1.97	18.11	0	11.21	0	0.58	0.10	0	0	0	0.428
2	AP6 Adipose			9.06	72.29	2.25	16.27	0	0	0	0	0.13	0	0	0	0.946
3	BR-12 Breast			8.59	70.10	2.33	17.90	0	0	0	0	0.13	0	0.95	0	0.981
4	Solid Water M457			8.02	67.22	2.41	19.91	0	0	0	0	0.14	0	2.31	0	1.045
5	LV1 Liver			8.06	67.01	2.47	20.01	0	0	0	0	0.14	0	2.31	0	1.095
6	SB3 Cortical Bone			3.41	31.41	1.84	36.50	0	0	0	0	0.04	0	26.81	0	1.823
7	*n*-Pentane	C_5H_{12}		16.76	83.24	0	0	0	0	0	0	0	0	0	0	0.626
8	*n*-Hexane	C_6H_{14}		16.37	83.63	0	0	0	0	0	0	0	0	0	0	0.659
9	*n*-Heptane	C_7H_{16}		16.09	83.91	0	0	0	0	0	0	0	0	0	0	0.683
10	Methanol	CH_4O		12.58	37.48	0	49.93	0	0	0	0	0	0	0	0	0.791
11	Ethanol	C_2H_6O		13.13	52.14	0	34.73	0	0	0	0	0	0	0	0	0.788
12	Propan-1-ol	C_3H_8O		13.42	59.96	0	26.62	0	0	0	0	0	0	0	0	0.805
13	Propan-2-ol	C_3H_8O		13.42	59.96	0	26.62	0	0	0	0	0	0	0	0	0.785
14	Oleic acid	$C_{18}H_{34}O_2$		12.13	76.54	0	11.33	0	0	0	0	0	0	0	0	0.892
15	Ethyl acetoacetate	$C_6H_{10}O_3$		7.74	55.37	0	36.88	0	0	0	0	0	0	0	0	1.026
16	Water	H_2O		11.19	0	0	88.81	0	0	0	0	0	0	0	0	0.998
17	Polyethylene glycol 200	C_2H_4O		9.15	54.53	0	36.32	0	0	0	0	0	0	0	0	1.123
18	Glycerol	$C_3H_8O_3$		8.76	39.13	0	52.12	0	0	0	0	0	0	0	0	1.260
19	Silicone oil Siluron 5000	C_2H_6OSi		8.16	32.39	0	21.58	0	0	0	37.87	0	0	0	0	0.970
20	Potassium Chloride 4.01%	KCl H_2O		10.74	0	0	85.25	0	0	0	0	1.91	2.10	0	0	1.021
21	Potassium Chloride 7.71%	KCl H_2O		10.33	0	0	81.97	0	0	0	0	3.67	4.04	0	0	1.046
22	Potassium Chloride 11.13%	KCl H_2O		9.94	0	0	78.92	0	0	0	0	5.29	5.84	0	0	1.070
23	Potassium Chloride 20.03%	KCl H_2O		8.95	0	0	71.02	0	0	0	0	9.53	10.51	0	0	1.139
24	Carbon graphite	C		0	100	0	0	0	0	0	0	0	0	0	0	1.696
25	UHMWPE	$(C_2H_4)_n$		14.37	85.63	0	0	0	0	0	0	0	0	0	0	0.923
26	Polypropylene	$(C_3H_6)_n$		14.37	85.63	0	0	0	0	0	0	0	0	0	0	0.919
27	Nylon 6.6-101	$(C_{12}H_{22}N_2O_2)_n$		9.80	63.68	12.38	14.14	0	0	0	0	0	0	0	0	1.142
28	PMMA	$(C_5H_8O_2)_n$		8.05	59.98	0	31.96	0	0	0	0	0	0	0	0	1.183
29	Polycarbonate	$(C_{16}H_{14}O_3)_n$		5.55	75.57	0	18.88	0	0	0	0	0	0	0	0	1.192
30	Teflon	$(C_2F_4)_n$		0	24.02	0	0	75.98	0	0	0	0	0	0	0	2.205
31	Aluminium $AlMgSi_1$			0	0	0	0	0	1	97.2	1	0	0	0	0.8	2.691
32	Al_2O_3 99.7%	Al_2O_3		0	0	0	47.07	0	0	52.93	0	0	0	0	0	3.892

$$\frac{S_m}{S_w} = \frac{\rho_e^m}{\rho_e^w}\left(\frac{f(\beta)-\ln\langle I_m\rangle}{f(\beta)-\ln\langle I_w\rangle}\right) \quad (7)$$

with the relative electron density ρ_e^m/ρ_e^w and mean excitation energy $\langle I_m\rangle$ of the material.

2.2. Specifications of the 32 materials

An overview of the 32 selected sample materials and their composition and density is given in Table 1. Material numbers 1–6 are 'tissue equivalent' (for CT photon energies) materials with specified compositions (Gammex Inc., Middleton, WI, USA). The analytical standards (No. 7-15, 17 and 18) were selected based on their high purity and well specified composition. Silicone oil (No. 19) is a material used as a tamponade after vitrectomy [24] in treatment of ocular tumours. Potassium chloride solutions (No. 20-23) were prepared to cover the intermediate atomic number (Z) range. In addition, different polymers (No. 25-30), aluminium and carbon were selected. Al_2O_3 (No. 32) is a ceramic used in prostheses. The samples of the solid materials were machined as 12 cm diameter disks with a thickness of approximately 2 cm water equivalent. The real thicknesses of the solid samples were measured at their centres and at 4 different points over a radius of 30 mm using a Sylvac Z_cal 300 m (Sylvac SA, Crissier) with an accuracy of 6 µm and precision of 2 µm. The solids were weighed on a Mettler PM6000 balance (Mettler-Toledo, LLC) with an accuracy of 0.05%. From the determined volume and mass, mass densities were calculated for the solid samples. The uncertainty in the measured thickness of the solid samples contributed almost a factor of ten more to the uncertainty in the mass densities than the uncertainty in the diameter, because of their difference in magnitude (thickness: 2 cm compared to diameter: 12 cm). The uncertainty in the mass was negligible. The uncertainty in the calculated densities was < 0.1% (except for PMMA and Teflon 0.3%) (1σ). Mass densities of the liquid samples were measured at room temperature using a DMA35N density meter (Anton Paar, Austria) with a specified accuracy of 0.001 g cm^{-3}. The temperatures of the water and measured samples during the proton experiments were 25.5 ± 0.3 to 25.8 ± 0.2 °C (ρ_w = 0.997 g cm^{-3}) and yielded an average deviation in the density of the liquid samples of −0.001 g cm^{-3} which was considered negligible. The densities of the samples *n*-pentane, *n*-hexane and *n*-heptane were taken from the specifications of the manufacturer.

2.3. Experimental depth dose distributions

2.3.1. Water phantom design

The water phantom (Fig. 1, left) is equipped with two parallel TSL 120 translation stages with a stroke length of 500 mm (IKO Japan, Nippon Thompson Europe BV). The stages, including a 5 phase stepping motor (VEXTA-PK566, Oriental Motors), have a positioning accuracy of 0.045 mm, a precision of 0.002 mm and a backlash of 0.003 mm. A polycarbonate holder was mounted to one of the stages to accurately move an ionization chamber along the beam for scanning a depth dose profile. A plane-parallel Markus ionization chamber type 23343 (PTW, Freiburg) was used as recommended by the TRS 398 report [25]. A sample can be positioned in a second polycarbonate holder which is mounted on the other stage. This stage allows changing the amount of water before the sample and thus the proton energy at the upstream side of the sample. In the measurements three different types of sample holders were used (two are shown in Fig. 1, right) namely, a circular windowless sample holder for solid samples that do not take up water (plastics, metals), a circular sample holder with polycarbonate windows for solid samples that might take up water (tissue equivalent lung, carbon) and a rectangular holder (nominal sample thickness: 20.3 mm), for the liquid samples. The Markus chamber was positioned downstream of the sample such that a depth dose profile could be measured. The absolute positions of the ionization chamber and sample were

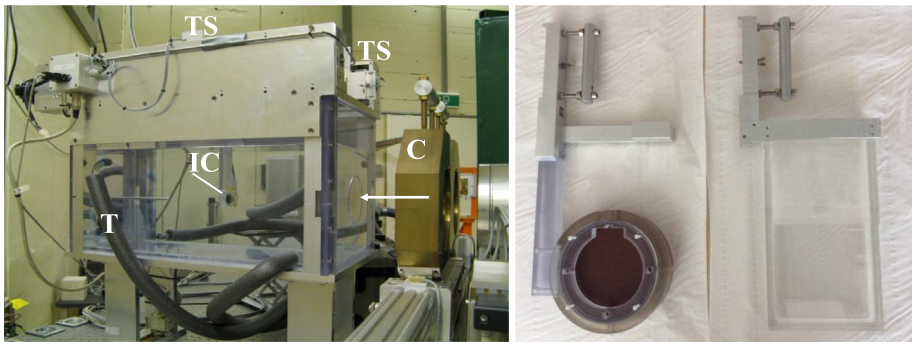

Fig. 1. Left figure: Experimental setup of the water phantom with its entrance window placed at the device under test (DUT) position. The arrow pointing to the entrance window indicates the beam direction. An ionization chamber (IC) is positioned in the water phantom on a translation stage (TS) to enable measurement of depth dose profiles. C and T indicate the 50 mm diameter field shaping collimator and the tubing of the water temperature stabilising system, respectively. Right figure: Sample holders for solid samples (left) and for liquid samples (right). The depicted solid sample holder is windowless and contains a tissue substitute sample of 12 cm diameter.

determined using MY-COM A30/80 limit switches (Baumer) with a precision < 1 μm. At the downstream side of the water phantom a PT100 temperature sensor is installed to measure the water temperature during the measurements. The readout of the PT100 is connected to a LabVIEW (National Instruments) program which also controls the operation of the stages and the beam and writes the measured data to output files. The entrance window of the water phantom is a 2.90 mm thick circular impression with a radius of 55 mm milled in a 14.86 mm thick polycarbonate plate. For the experiments, the water phantom was filled with demineralized water. The water temperature was stabilized to 25.5 ± 0.3 °C by circulating the water through a temperature regulated thermal buffer.

2.3.2. Proton beamline and experimental setup

The AGOR cyclotron [26] produces a 190 MeV (nominal) proton pencil beam with a full width at half maximum (FWHM) of 4 mm. The beam has an energy spread of 0.25% FWHM. The protons exit the vacuum of the beam pipe through a 70 μm thick aramica foil and then are incident on a homogeneous 1.44 mm thick Pb scatter foil. Two collimators (diameters 2.4 cm and 4.5 cm) shape the scattered field. Thereafter the beam intensity is measured with a parallel plate air ionization monitor (BIM: beam intensity monitor). A third collimator removes the halo from the proton field after which a collimator with an inner diameter of 50 mm determines the final shape of the field. The proton field at the device under test (DUT) position (at 329.6 cm distance from the exit foil) has been imaged to determine the field flatness using a scintillation screen (Gd_2O_2S:Tb, Lanex™, Eastman Kodak Company, Rochester, NY). This scintillation screen is placed perpendicular to the beam direction and is imaged via a mirror reflecting light at a 90° angle to a CCD camera [27]. For measurement of depth dose profiles, the entrance window of the water phantom has been placed at the DUT position.

2.3.3. Measurement and analysis of depth dose distributions

Four experiments (of approximately 18 h beam time each) were needed to measure the depth dose distributions downstream of all of the 32 samples at the position in the water phantom that corresponded to a proton energy of 149 MeV. For selected samples also depth dose distributions at positions corresponding to 62 and 89 MeV were measured. In all these experiments firstly the field flatness has been verified. Thereafter, the depth dose distributions have been measured with a step size of 5 mm in the plateau region and 0.2 mm in the Bragg peak by administering a dose of 0.5 to 1 Gy per point. For all samples one full depth dose distribution was measured (taking about 10 min) and two distributions in the region starting just upstream of the Bragg peak (taking about 7 min each). Furthermore, at regular intervals in time a depth dose distribution without a sample was measured for reference. The measured depth dose distributions have been corrected for background in both the BIM and the Markus chamber reading using the time intervals counted with a fixed frequency pulser. The proton range has been defined as the distal 80% of the maximum dose in the Bragg peak ($R_{80\%}$). At this point, 50% of the protons have stopped independent of the energy spread of the beam [28–30]. The Bragg peaks measured with a step size of 0.2 mm have been interpolated with a cubic spline interpolation. From the splined Bragg peak, the local maximum has been defined as the position at which the first derivative of the spline equals zero and the signal has been normalized to this local maximum. For a sample measurement a range shift ΔR can be determined from the difference in $R_{80\%}$ between the measurement in water with and without the sample positioned in the water. The water equivalent thickness (t_w, WET) is derived from $t_w = t_m - \Delta R$ with t_m the sample thickness. The sign of the range shift ΔR is positive in case the range with sample is longer than the range without sample. The water equivalent ratio (WER, t_w/t_m) is considered as the relative stopping power (RSP) of the sample. The data analysis has been implemented in a commercially available software package (MATLAB 8.3, The MathWorks Inc., Natick, MA, USA). This analysis method to determine experimental RSPs has been applied to the samples of the 32 materials.

During operation, the cyclotron magnetic field slowly drifts in the order of a hundredth of a percent over a period of around 24 h due to warming up of the iron poles. Due to this drift there is a slow change in energy of the beam. Fig. 2 presents the measured ranges ($R_{80\%}$) as a function of time during one of the experiments. The reproducibility of the $R_{80\%}$ in water during the four performed experiments was within 0.058 mm, 0.095 mm, 0.052 mm and 0.071 mm. The variations in beam energy limit the reproducibility of depth dose distributions in water. This reproducibility is essential for accurate measurement of the range shift between a Bragg curve measured after a sample and a measurement in water only. For these range shift measurements the nearest measured depth dose distribution in water has been used to reduce the variation in the reference water measurement since the energy drifts only slowly between two depth dose measurements in water.

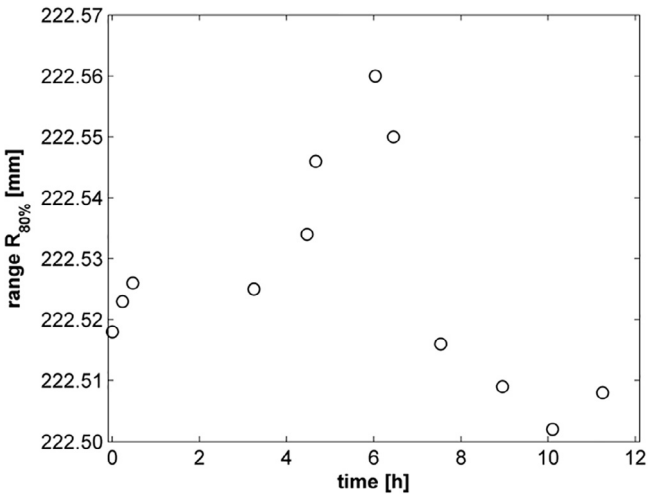

Fig. 2. The range ($R_{80\%}$) of protons in water corresponding to the extraction energy of 189.3 MeV as a function of time during one of the experiments. Error bars are within markers of the data points.

2.3.4. Geant4 simulations

The experimental proton beamline from the exit foil to the DUT position has been modelled in Geant4 (Geant4.9.6.p04, [31]). At the DUT position the water phantom is represented by a polycarbonate front wall including the entrance window followed by a water column of 25 × 25 × 55 cm^3. A proton beam with the specifications listed in Section 2.3.2 has been simulated starting just upstream of the exit foil. For the mean excitation energy of water $\langle I_w \rangle$ a value of 78 eV has been adopted corresponding to the updated ICRU 73 value [32]. The density of water ρ_w has been set at 0.997 g cm^{-3} corresponding to the density of water during the experiments. The physics list in simulations uses the settings of the TOPAS beta version v1.0b12 [33] with a range cut value of 0.05 mm for all particles.

The flatness of the transverse profile of the radiation field as a function of depth in the water phantom has been simulated to assess if the proton field can be considered uniform at the surface of the Markus chamber at all depths of the depth dose profile. Furthermore, depth dose distributions in water with and without a sample were simulated. The composition and density of the samples used in the simulations were taken from Table 1. The dose has been scored as a function of depth in water with a bin size (in depth) of 0.1 mm and integrated over a radius (lateral) of 10 mm. The simulated depth dose data has been interpolated with a third order spline and normalized using the same method as applied to the experimental data.

3. Results and discussion

3.1. Experiments and Monte Carlo simulations

The Lanex scintillation screen images and the Geant4 simulations showed that the flatness of the field for a 10 mm radius is within 3% up to a depth of the $R_{80\%}$ in water. This justifies the use of the Markus ionization chamber with a 5.3 mm diameter electrode for measurement of depth dose distributions and the choice of the 10 mm radius of the dose scoring volume in the simulations.

The simulations have been checked on consistency with the experiments by determining the difference between a Geant4 simulated depth dose distribution and experimentally measured depth dose distributions in water. The nominal proton energy of 190 MeV in the simulations has been adjusted to 189.3 MeV by minimizing the range difference between the simulation and experiments and is in good correspondence with calculations of the beam dynamics in the cyclotron. Geant4 simulated and measured depth dose distributions in water for the first experiment are presented in Fig. 3 (top). The differences between the Geant4 simulated depth dose distribution and the depth dose distributions measured in the 4 performed experiments are smaller than 3% up to the $R_{80\%}$ (Fig. 3 bottom). In the distal falloff of the Bragg curve (after the $R_{80\%}$) where the energy of the protons becomes small, the differences between simulation and experiments increase. It should be noted, however, that in the steep distal fall off, small differences in the depth will already lead to large differences in the ratio between simulation and experiment.

3.2. Uncertainties in experimental relative stopping power determination

Experimental determination of proton relative stopping powers of materials is subject to different sources of uncertainty. A first uncertainty is the energy stability of the proton beam in between the reference water measurement and the sample measurement as mentioned in the previous section. A change in energy translates in a measured range difference and restricts the reproducibility of the measured range in water. The mechanical uncertainty in the ionisation chamber measurement is assumed to be negligible since the precision of the stepping motor is specified at 2 μm and the precision of the limit switches < 1 μm. The uncertainty associated with the reproducibility of the measured range in water, σ_R, can be estimated by $a/\sqrt{3}$ [34] with a the maximum difference between the $R_{80\%}$ in the measured Bragg curve in water used as reference for the sample measurement and the $R_{80\%}$ in the previous and following measured Bragg curves in water. The relative stopping power is given by the ratio t_w/t_m which equals $(t_m - \Delta R)/t_m$ with t_w the water equivalent thickness of the sample, t_m the material thickness and ΔR the measured range difference of the sample measurement relative to water. The uncertainty in the determined relative stopping powers depends on ΔR and t_m and their uncertainties. With the described setup, an uncertainty associated with the reproducibility of the measured range in water $\sigma_R < 31$ μm has been achieved in all four performed experiments, leading to an uncertainty in $\Delta R < 44$ μm. Including the uncertainty in the thickness measurements the experimental RSPs have been determined with a relative standard uncertainty [34] smaller than 0.4% for 32 samples with a water equivalent thickness of about 2 cm (Table 2, fourth column). To achieve even lower uncertainty levels, a higher energy stability of the proton beam is needed to reduce the contribution of σ_R and the sample thickness should be known with micrometre accuracy for samples with thicknesses in the order of 1 to 2 cm. Increasing the thickness of the samples would highly contribute to a reduction in the uncertainty of the measured RSP. This would, however, result in an RSP being averaged over a larger energy range, for $t_w = 2$ cm the energy of 149 MeV at the upstream side of the sample is already reduced to 138 MeV at the downstream side. Moreover, the multiple Coulomb scattering would be different as compared to the situation of water only. For soft tissues with an RSP around 1.0 these effects might be small but for lung, bone and metals they are pronounced.

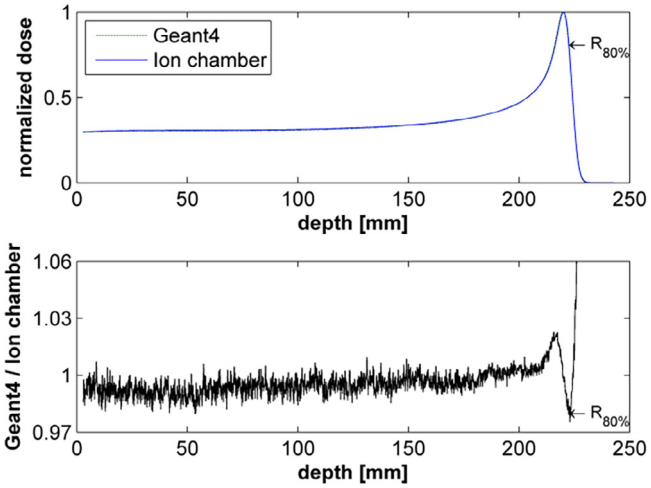

Fig. 3. Comparison between Geant4 simulated and ionisation chamber measured depth dose distributions in water for experiment 1. The two curves nearly overlap (top figure) and the difference between the Geant4 simulated and the experimentally measured depth dose distribution is within 3% up to a depth corresponding to the range ($R_{80\%}$).

Another source of uncertainty is the possible influence of neutrons on the dose measurements. Neutrons are inevitably produced by the proton beam both in the beam shaping elements (scatter foil, collimators) and in the water phantom and sample. As in this study range shifts were measured, only the influence of the sample on the neutron fluence has to be considered (all other neutron sources are present during both the measurement with and without sample). As we use relatively thin (with respect to the amount of water traversed) targets the influence is expected to be small. Moreover, in an absolute sense, the neutron induced dose fraction for proton beams in the energy range of 160–250 MeV is small and has been calculated to be approximately 0.3% in the plateau and 0.1% in the Bragg peak region [35] and a few centimetres distal from the Bragg peak to reduce to only 0.04% [36]. This implies that any influence of dose due to neutrons on the range shift measurements is negligible.

Table 2
The measured thickness t_m (± 1 standard deviation) of the 32 sample materials. Experimental relative stopping powers (RSP Exp) determined with an uncertainty < 0.4% at an initial proton energy of 149 MeV compared to RSPs derived from the Bethe-Bloch approximation with Bragg additivity rule (BB), with mean excitation energy for water set to 78 eV (BB(78)) and from Geant4 simulations (RSP Geant4). In the last column the measured water equivalent thickness t_w of the samples is given.

No.	Material	t_m [mm]	RSP Exp	RSP BB	RSP BB (78)	RSP Geant4	t_w [mm]
1	LN-450 Lung	46.977 ± 0.007	0.421	0.416	0.422	0.423	19.777
2	AP6 Adipose	22.017 ± 0.009	0.951	0.936	0.950	0.949	20.938
3	BR-12 Breast	21.033 ± 0.008	0.979	0.964	0.979	0.980	20.591
4	Solid Water M457	19.99 ± 0.01	1.033	1.018	1.034	1.032	20.65
5	LV1 Liver	20.014 ± 0.009	1.084	1.067	1.083	1.082	21.695
6	SB3 Cortical Bone	12.94 ± 0.01	1.622	1.628	1.652	1.656	20.99
7	*n*-Pentane	20.31 ± 0.10	0.684	0.679	0.689	0.687	13.89
8	*n*-Hexane	20.31 ± 0.10	0.717	0.711	0.722	0.723	14.56
9	*n*-Heptane	20.31 ± 0.10	0.740	0.735	0.746	0.745	15.03
10	Methanol	20.32 ± 0.09	0.816	0.810	0.822	0.824	16.58
11	Ethanol	20.32 ± 0.09	0.822	0.815	0.827	0.826	16.70
12	Propan-1-ol	20.32 ± 0.09	0.841	0.836	0.849	0.847	17.09
13	Propan-2-ol	20.32 ± 0.09	0.822	0.816	0.828	0.829	16.70
14	Oleic acid	20.28 ± 0.09	0.920	0.916	0.930	0.928	18.66
15	Ethyl acetoacetate	20.32 ± 0.09	1.003	0.995	1.010	1.009	20.38
16	Water	20.28 ± 0.09	1.000	1.000	1.015	1.000	20.28
17	Polyethylene glycol 200	20.28 ± 0.09	1.115	1.108	1.125	1.124	22.61
18	Glycerol	20.31 ± 0.10	1.238	1.233	1.252	1.252	25.14
19	Silicone oil Siluron 5000	19.815 ± 0.000	0.926	0.916	0.930	0.932	18.349
20	Potassium Chloride 4.01%	20.28 ± 0.09	1.014	1.011	1.027	1.028	20.56
21	Potassium Chloride 7.71%	20.28 ± 0.09	1.025	1.027	1.043	1.044	20.79
22	Potassium Chloride 11.13%	20.28 ± 0.09	1.043	1.042	1.058	1.058	21.15
23	Potassium Chloride 20.03%	20.28 ± 0.09	1.084	1.086	1.102	1.104	21.98
24	Carbon graphite	12.03 ± 0.01	1.518	1.504	1.526	1.521	18.26
25	UHMWPE	18.18 ± 0.02	0.994	0.974	0.989	0.987	18.07
26	Polypropylene	18.962 ± 0.007	0.979	0.970	0.985	0.984	18.564
27	Nylon 6.6-101	15.96 ± 0.02	1.148	1.140	1.157	1.160	18.32
28	PMMA	15.94 ± 0.04	1.168	1.153	1.171	1.170	18.62
29	Polycarbonate	15.93 ± 0.02	1.140	1.130	1.147	1.145	18.10
30	Teflon	10.59 ± 0.03	1.788	1.811	1.838	1.841	18.94
31	Aluminium $AlMgSi_1$	8.96 ± 0.01	2.129	2.087	2.119	2.123	19.08
32	Al_2O_3 99.7%	7.089 ± 0.001	3.198	3.185	3.233	3.238	22.67

3.3. Comparison of experimental and calculated values

In Table 2 the RSPs measured at 149 MeV proton energy are compared with RSPs calculated from the approximation of the Bethe-Bloch formula given in Eq. (7). RSPs were calculated with mean excitation energies derived from the composition with Bragg's additivity rule for all materials (Table 2, 5th column, RSP BB). The elemental mean excitation energies were taken from ICRU [19,20]. An identical calculation was done except that for the denominator the mean excitation energy of water was set at 78 eV (Table 2, 6th column, RSP BB(78)) to enable an equal based comparison with the RSPs calculated from the Geant4 simulations that also used a $\langle I_w \rangle$ = 78 eV (Table 2, 7th column, RSP Geant4).

Fig. 4 presents the relative difference of the three calculated RSPs data sets with the experimental RSPs as a function of the density of the sample. From the figure we conclude that all three calculated data sets show the same pattern in their relative differences with the experimental values, the data sets are only shifted in the vertical direction. The shift between the RSPs BB and RSPs BB(78) is due to setting $\langle I_w \rangle$ = 78 eV instead of calculating the value using Bragg's additivity rule (resulting in $\langle I_w \rangle$ = 69 eV). This shift is approximately 1.5% in Fig. 4. Comparing the RSPs BB(78) with the RSPs Geant 4 in Table 2 and their difference with the experiment values we observe that these two data sets are almost identical, in fact the differences are less than 0.3% for all 32 materials. From this it can be concluded that the correction terms in the Bethe-Bloch formula can be safely neglected for a large set of materials at proton energies in the therapeutical domain.

Considering the experimental RSPs as the ground truth values it is rather disappointing that none of the calculated data sets is unbiased. From Table 3 we conclude that the RSPs BB underestimate the

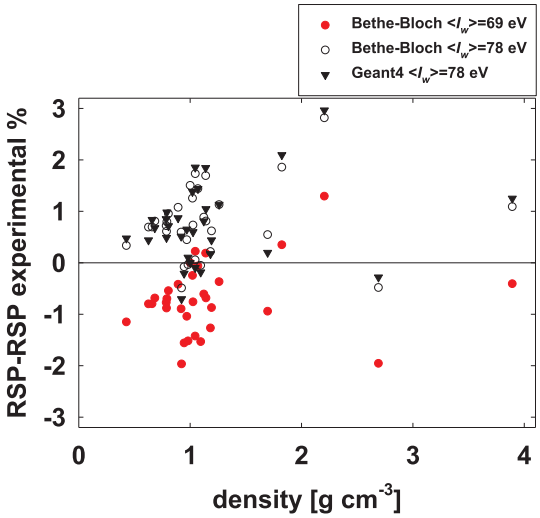

Fig. 4. Relative difference between experimental RSPs and RSPs predicted by the approximate Bethe-Bloch formula with $\langle I_w \rangle$ = 69 eV and 78 eV, respectively and predicted from Geant4 simulations with $\langle I_w \rangle$ = 78 eV.

experimental values with 0.7% while the RSPs BB(78) and the RSPs Geant4 overestimate with 0.7–0.8%. In these estimates the values taken for the mean excitation energy of water seems to be the major source of the bias, in fact, taking a value of $\langle I_w \rangle$ = 3.2 eV would result in an unbiased estimate (BB(73.2) in Table 3) for the data set of 32 materials. This value of $\langle I_w \rangle$ is in the range of values from the literature 67–82 eV [37,38]. Recently, Doolan et al [39] derived a set of optimized

Table 3
Mean and standard deviation (std) of the relative difference of the BB, BB(78), Geant4 and BB (73.2) RSP data sets with the experimental RSPs.

Data set RSP	mean ± std (%)
BB	−0.7 ± 0.7
BB(78)	0.8 ± 0.7
Geant4	0.7 ± 0.8
BB(73.2)	0.0 ± 0.7

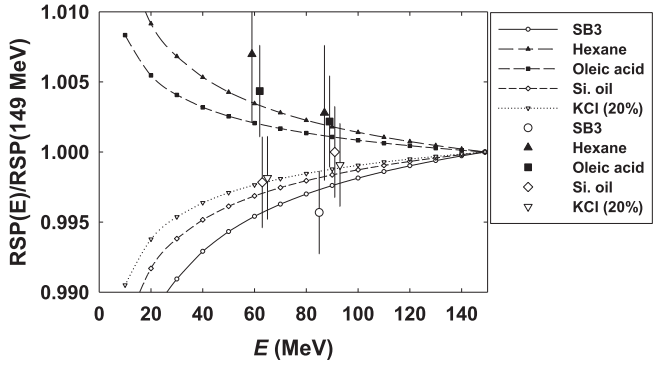

Fig. 5. Ratios of relative stopping powers at energy E and at energy 149 MeV. Lines and small symbols depict these ratios on basis of the approximate Bethe-Bloch formula and the composition of the materials and the large symbols with error bars reflect the measured ratios. The five materials in the figure are nr. 6, 8, 14, 19 and 23 in Tables 1 and 2.

elemental $\langle I \rangle$-values based on matching experimental and calculated stopping powers for 11 Gammex tissue substitute materials. Using these optimize values and the Bragg additivity rule yields $\langle I_w \rangle = 73.9$ eV which is in close agreement with the value $\langle I_w \rangle = 73.2$ eV we deduce for an unbiased calculated data set based on 32 materials.

The energy dependence of the RSPs relative to their RSP value at 149 MeV is plotted for five materials in Fig. 5 both for RSPs predicted from the Bethe-Bloch formula and the materials composition and for experimental RSPs. The figure shows that within the uncertainties the predicted curves and the experimental data agree and in all cases the predicted upward or downward trend with decreasing energy is consistent with the experimental values. The energy dependence of the RSPs is smaller than 0.5% and can be neglected in the current clinical practice where uncertainties due to translation of single energy CT information to stopping powers are larger than 1% [40]. However, in the development of high accuracy RSP prediction using dual energy CT [4–10] and/or proton radiography or proton CT [41] the accuracy of the RSP estimation may reach the subpercent level and then the energy dependence should be accounted for.

3.4. Comparison with other experimental setups

Different methods to measure relative stopping powers have been presented in literature. Schaffner and Pedroni [2] measured depth dose profiles using range shifter plates to degrade the proton beam energy. The water equivalent thickness of the range shifter plates was 2.3 mm which limits the spacing of the Bragg curve measurements. With this setup they expected an accuracy of the measured range shift of ± 0.1 range shifter plate corresponding to an accuracy of 0.2% in the RSP measurement for 10 cm thick tissue samples. For samples with a thickness of 2 cm this accuracy would amount to about 1%. Witt et al. [42] have employed the PTW Peakfinder (PTW, Freiburg, Germany) for residual range measurements with a specified uncertainty in the residual range measurement of 50 μm. For 7 cm thick samples they estimated the uncertainty in the measured RSP to be < 0.3%. Jäkel et al. [43] and Hünemohr et al. [10] have used a slightly different design of the PTW Peakfinder and reported an accuracy in the measured relative water equivalent shifts of Bragg peak positions for samples between 1 and 3.5%. Recently, Möhler et al. [44] presented a RSP measurement method with 0.1% or better accuracy for 1.78 cm thick biological materials in a 3D printed container with equal sized sample compartments. This method uses that the container is very precisely printed and the thicknesses of both the sample and the water and air references can be assumed identical and cancel in the RSP calculation. In fact, the 3D printer used in their study (Objet30 Pro) only has an accuracy of 100 μm [45], however, the precision of 3D printing centimetre sized PMMA objects is approximately 0.2% [46] which seems the limiting factor in the accuracy of the method. This is reflected by the fact that for a single sample measurement (instead of averaging over 5 samples) the accuracy would be of the order of 0.2% ($\sqrt{5}$ times 0.1%). This makes the method of Möhler et al. for single sample measurements slightly better than our method, however, in case the accuracy of our sample thickness definition is improved by a factor of two both methods have comparable accuracy.

The accuracy in determining relative proton stopping powers from residual range measurements achieved with our water phantom (uncertainty < 0.4% for samples with 2 cm water equivalent thickness) is better or comparable to most of the other presented systems. The large sample thicknesses (about 10 cm) used in the studies of Schaffner and Pedroni [2] and Witt et al. [42] strongly reduce their uncertainty in the relative stopping power measurements but have disadvantages concerning energy definition and multiple coulomb scattering (see Section 4.2).

4. Conclusions

We have developed a water phantom for accurate depth dose measurements. The uncertainty associated with the reproducibility of the measured range in water is determined by the energy stability of the proton beam. The instrument allows relative proton stopping powers to be measured with accuracy better than 0.4% by measuring range differences in water for samples with a water equivalent thickness of about 2 cm. This achieved accuracy is sufficient for experimental validation of relative stopping powers predicted by computed tomography or Monte Carlo simulations for particle therapy.

With the water phantom RSPs of a large set of materials were accurately measured. These experimental RSPs allowed us to conclude that using in the Bethe Bloch equation for the mean excitation energy of water $\langle I_w \rangle$ the value from Bragg's additivity rule ($\langle I_w \rangle$=69 eV) or the updated ICRU 73 value ($\langle I_w \rangle$=78 eV) leads to an underestimate and an overestimate, respectively, with approximately 0.7%, of the experimental values. Considering the value of $\langle I_w \rangle$ as the main source of this bias we derived an optimized value of $\langle I_w \rangle$=73.2 eV from our data set.

In this study we found that, in the clinically relevant energy range, the energy dependence of RSPs is smaller than 0.5% and can be neglected in the current clinical practice where uncertainties in stopping powers are larger than 1%. However, in case of improved accuracy of RSP estimation, with e.g. combinations of photon and proton imaging, taking the energy dependency into account may be required.

Acknowledgements

This research has been in part funded by the 'Stichting voor Fundamenteel Onderzoek der Materie (FOM)', which is financially supported by the 'Nederlandse Organisatie voor Wetenschappelijk Onderzoek (NWO)' and by Siemens Healthcare (Forchheim, Germany).

References

[1] R.R. Wilson, Radiological use of fast protons, Radiology 47 (1946) 487–491.
[2] B. Schaffner, E. Pedroni, The precision of proton range calculations in proton radiotherapy treatment planning: experimental verification of the relation between CT-HU and proton stopping power, Phys. Med. Biol. 43 (1998) 1579–1592.
[3] U. Schneider, E. Pedroni, A. Lomax, The calibration of CT Hounsfield units for radiotherapy treatment planning, Phys. Med. Biol. 41 (1996) 111–124.
[4] M. Torikoshi, T. Tsunoo, M. Sasaki, M. Endo, Y. Noda, Y. Ohno, T. Kohno, K. Hyodo, K. Uesugi, N. Yagi, Electron density measurement with dual-energy X-ray CT using synchrotron radiation, Phys. Med. Biol. 48 (2003) 673–685.
[5] M. Bazalova, J.-F. Carrier, L. Beaulieu, F. Verhaegen, Dual-energy CT-based material extraction for tissue segmentation in Monte Carlo dose calculations, Phys. Med. Biol. 53 (2008) 2439–2456.
[6] M. Saito, Potential of dual-energy subtraction for converting CT numbers to electron density based on a single linear relationship, Med. Phys. 39 (2012) 2021–2030.
[7] G. Landry, J. Seco, M. Gaudreault, F. Verhaegen, Deriving effective atomic numbers from DECT based on a parameterization of the ratio of high and low linear attenuation coefficients, Phys. Med. Biol. 58 (2013) 6851–6866.
[8] M. Tsukihara, Y. Noto, T. Hayakawa, M. Saito, Conversion of the energy-subtracted CT number to electron density based on a single linear relationship: an experimental verification using a clinical dual-source CT scanner, Phys. Med. Biol. 58 (2013) N135–N144.
[9] J.K. van Abbema, M.-J. van Goethem, M.J.W. Greuter, A. van der Schaaf, S. Brandenburg, E.R. van der Graaf, Relative electron density determination using a physics based parameterization of photon interactions in medical DECT, Phys. Med. Biol. 60 (2015) 3825–3846.
[10] N. Hünemohr, B. Krauss, C. Tremmel, B. Ackermann, O. Jäkel, S. Greilich, Experimental verification of ion stopping power prediction from dual energy CT data in tissue surrogates, Phys. Med. Biol. 59 (2014) 83–96.
[11] A.E. Bourque, J.-F. Carrier, H. Bouchard, A stoichiometric calibration method for dual energy computed tomography, Phys. Med. Biol. 59 (2014) 2059–2088.
[12] H. Bichsel, Shell corrections in stopping powers, Phys. Rev. A 65 (2002) 052709–1–11.
[13] J.F. Ziegler, Stopping of energetic light ions in elemental matter, J. Appl. Phys. 85 (1999) 1249–1272.
[14] J.F. Ziegler, J.P. Biersack, M.D. Ziegler, SRIM The Stopping and Range of Ions in Matter, SRIM Co., Chester, MD, 2008.
[15] H. Bichsel, Stopping power and ranges of fast ions in heavy elements, Phys. Rev. A 46 (1992) 5761–5773.
[16] J.C. Ashley, R.H. Ritchie, W. Brandt, Z_1^3 effect in the stopping power of matter for charged particles, Phys. Rev. B 5 (1972) 2393–2397.
[17] W.H. Bragg, R. Kleeman, On the α particles of radium, and their loss of range in passing through various atoms and molecules, Philos. Mag. Series 6 (10) (1905) 318–340.
[18] P. Bauer, D. Semrad, Chemical and physical state effects in electronic stopping, in: Theory of the Interaction of Swift Ions with Matter, vol. 46, Part 2 of Advances in Quantum Chemistry, Academic Press, 2004, pp. 153–163.
[19] ICRU, Stopping powers for electrons and positrons, Report No. 37, ICRU, Bethesda, MD, USA, 1984.
[20] ICRU, Stopping powers for protons and alpha particles, Report No. 49, ICRU, Bethesda, MD, USA, 1993.
[21] H. Bichsel, T. Hiraoka, Energy loss of 70 MeV protons in elements, Nucl. Instr. Methods Phys. Res. Sect. B: Beam Interact. Mater. Atoms 66 (1992) 345–351.
[22] Hiraoka, K. Kawashima, K. Hoshino, A. Fukumura, H. Bichsel, Energy loss of 70 MeV protons in organic polymers, Med. Phys. 20 (1993) 135–141.
[23] M.J. Berger, J.S. Coursey, M.A. Zucker, J. Chang, ESTAR, PSTAR, and ASTAR: Computer Programs for Calculating Stopping-Power and Range Tables for Electrons, Protons, and Helium Ions (version 1.2.3). [Online] Available: http://physics.nist.gov/Star [2016 03 30], 2005.
[24] M.J. Berger, J.S. Coursey, M.A. Zucker, J. Chang, ESTAR, PSTAR, and ASTAR: Computer Programs for Calculating Stopping-Power and Range Tables for Electrons, Protons, and Helium Ions (version 1.2.3). [Online] Available: http://physics.nist.gov/Star [2016 03 30], 2005.
[25] IAEA, Absorbed dose determination in external beam radiotherapy: an international code of practice for dosimetry based on standards of absorbed dose to water, Technical Reports Series 398, International Atomic Energy Agency, 2000.
[26] E.R. van der Graaf, R.W. Ostendorf, M.-J. van Goethem, H.H. Kiewiet, M.A. Hofstee, S. Brandenburg, AGORFIRM, the AGOR facility for irradiations of materials, in: Proceedings 10th European Conference on Radiation Effects on Components and Systems, 14–18 September, 2009, Bruges, Belgium (2009), 451–454.
[27] S.N. Boon, P. van Luijk, J.M. Schippers, H. Meertens, J.M. Denis, S. Vynckier, J. Medin, E. Grusell, Fast 2D phantom dosimetry for scanning proton beams, Med. Phys. 25 (1998) 464–475.
[28] B. Gottschalk, Physics of proton interactions in matter, in: H. Paganetti (Ed.), Proton Therapy Physics, CRC Press, Boca Raton, 2012, pp. 19–60.
[29] S.-Y. Cai, T.-C. Chao, M.-J. Lin, C.-J. Tung, C.-C. Lee, Depth dose characteristics of proton beams within therapeutic energy range using the particle therapy simulation framework (PTSim) Monte Carlo technique, Biomed. J. 38 (2015) 408–413.
[30] H. Paganetti, Range uncertainties in proton therapy and the role of Monte Carlo simulations, Phys. Med. Biol. 57 (2012) R99–R117.
[31] S. Agostinelli, et al., Geant4: a simulation toolkit, Nucl. Instr. Methods Phys. Res. A 506 (2003) 250–303.
[32] P. Sigmund, A. Schinner, H. Paul, Errata and Addenda for ICRU Report 73, Stopping of ions heavier than helium, ICRU, 2009.
[33] J. Perl, J. Shin, J. Schümann, B. Faddegon, H. Paganetti, TOPAS: an innovative proton Monte Carlo platform for research and clinical applications, Med. Phys. 39 (2012) 6818–6837.
[34] JCGM/WG 1, Evaluation of measurement data – Guide to the expression of uncertainty in measurement, JCGM 100:2008, Joint Committee for Guides in Metrology, 2008.
[35] J. Mulder, Water calorimetry for proton therapy, implementing a primary dose measurement standard, PhD thesis, University of Groningen, 2017.
[36] H. Paganetti, Nuclear interactions in proton therapy: dose and relative biological effect distributions originating from primary and secondary particles, Phys. Med. Biol. 47 (2002) 747–764.
[37] P. Andreo, On the clinical spatial resolution achievable with protons and heavier charged particle radiotherapy beams, Phys. Med. Biol. 54 (2009) N205–N215.
[38] H. Paul, The stopping power of matter for positive ions, in: G. Natanasabapathi (Ed.), Modern Practices in Radiation Therapy, Intech, 2012, pp. 113–132.
[39] P.J. Doolan, C.-A. Collins-Fekete, M.F. Dias, T.A. Ruggieri, D. D'Souza, J. Seco, Inter-comparison of relative stopping power estimation models for proton therapy, Phys. Med. Biol. 61 (2016) 8085–8104.
[40] J. Schuemann, S. Dowdell, C. Grassberger, C.H. Min, H. Paganetti, Site-specific range uncertainties caused by dose calculation algorithms for proton therapy, Phys. Med. Biol. 59 (2014) 4007–4031.
[41] R.P. Johnson, Review of medical radiography and tomography with proton beams, Rep. Prog. Phys. 81 (2018) 016701.
[42] M. Witt, U. Weber, D. Kellner, R. Engenhart-Cabillic, K. Zink, Optimization of the stopping-power-ratio to Hounsfield-value calibration curve in proton and heavy ion therapy, Z. Med. Phys. 25 (2015) 251–263.
[43] O. Jäkel, C. Jacob, D. Schardt, C.P. Karger, G.H. Hartmann, Relation between carbon ion ranges and X-ray CT numbers, Med. Phys. 28 (2001) 701–703.
[44] C. Möhler, T. Russ, P. Wohlfahrt, A. Elter, A. Runz, C. Richter, S. Greilich, Experimental verification of stopping-power predication from single- and dual-energy computed tomography in biological tissues, Phys. Med. Biol. 63 (2018) 025001.
[45] Objet30 pro, datasheet, https://proto3000.com/objet-30-pro.php#Tabs:Specifications, last accessed 18-7-2018.
[46] C. Polzin, S. Spath, H. Seitz, Characterization and evaluation of a PMMA-based 3D printing process, Rapid Prototyping J. 19 (2011) 37–43.